Supplementary materials

S.1 Identification of the bore tail

The method employed for identifying the beginning of the bore tail is the same as that used in Barranco & Liu (2021). A histogram of the normalized free surface elevation, η/η_{max}, is constructed for each time history. For each time record only values $\eta/h_0 \geqslant 0.05$ are taken into consideration to build the histogram. The bin size used in the histogram is 0.05 with 50% overlapping. The bin that has the highest percentage of occurrence represents the bore plateau. The last measurement (in time) within this bin is designated as the beginning of the bore tail. This methodology is generally robust for long bores. However, for short bores, the beginning of the bore tail can be miss-identified.

For illustration, the time histories of dimensionless free surface elevations at CG1 and the histograms of the free surface elevation records for case $L_p/h_0 = 20$ and $F_{in} = 1.3$ are plotted in figures S1 and S2, respectively. The bore presents an undulating front which converges towards the bore plateau, in which the leading undulation is twice the height of the bore plateau. The height of the bore plateau is easily identified by the histogram. The time histories of dimensionless free surface elevations at CG4 and the histograms of the free surface elevation records for the same case are plotted in figures S3 and S4, respectively. As the bore propagates, the length of the bore decreases and undulations may grow in the bore tail for short UBs and UBBs. At CG4 the bore plateau is not easily recognized from the free surface time history. On the other hand, the histogram points out the dimensionless height of the bore is between 0.225 and $0.275\eta/\eta_{max}$, which corresponds to one of the more flat undulations following the undulating front.

For short and decaying BBs a similar problem arises in the identification of the bore tail beginning. The time histories of dimensionless free surface elevations at CG1 and the histograms of the free surface elevation records for case $L_p/h_0 = 33.33$ and $F_{in} = 1.7$ are plotted in figures S5 and S6, respectively. The bore presents a steep front followed by an almost constant bore height until the beginning of the bore tail. The height of the bore plateau is easily identified by the histogram between 0.925 and $0.975\eta/\eta_{max}$. The time histories of dimensionless free surface elevations at CG4 and the histograms of the free surface elevation records for the same case are plotted in figures S3 and S4, respectively. At CG4 the tail of the bore has reached the bore front (there is no noticeable bore plateau), indicating the bore has started to decay. The histogram points out the dimensionless height of the bore is between 0 and $0.055\eta/\eta_{max}$, which corresponds to the flat surface after the bore tail has passed.

The laboratory results show that the method proposed in Barranco & Liu (2021) can miss-identify the beginning of the bore tail for short and decaying bores (not present in their study). Based on the laboratory results, only the dimensionless free surface heights above $0.4\eta_{max}/h_0$ in the histogram are taking in consideration for bore strength $F < 1.35$ (in which the leading undulations have been observed to be up to twice the bore height). For bore strength $F \geqslant 1.35$, for which the undulations are smaller, this minimum height limit is set at $0.75\eta_{max}/h_0$.

S.2 Arrival time of a bore front

The data scattering of the bores strength F_{12} and F_{toe} for the cases with $F_{in} = 1.9$ and $F_{in} = 1.1$, respectively, is analyzed in this section. The detail of the bore arrivals at CG1 and CG2 for cases $F_{in} = 1.9$ is shown in figure S9. All the cases have been synchronized with the arrival times at CG1. While the case $L_p/h_0 = 20$ takes 3.26 $t\sqrt{g/h_0}$ to reach CG2, resulting in a strength $F_{12} = 2.05$, the case $L_p/h_0 = 33.33$ takes 3.82 $t\sqrt{g/h_0}$

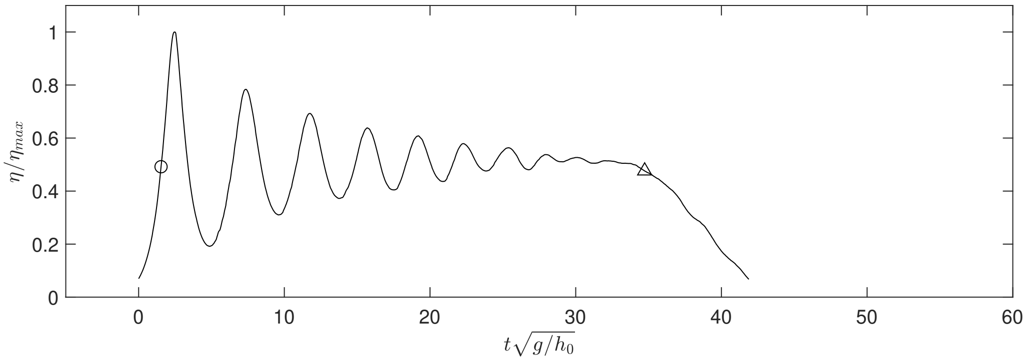

FIGURE S1. Time history of dimensionless free surface elevations at CG1 for $L_p/h_0 = 20$ and $F_{in} = 1.3$. Triangle marks the beginning of the bore tail and circle the first point with the same amplitude.

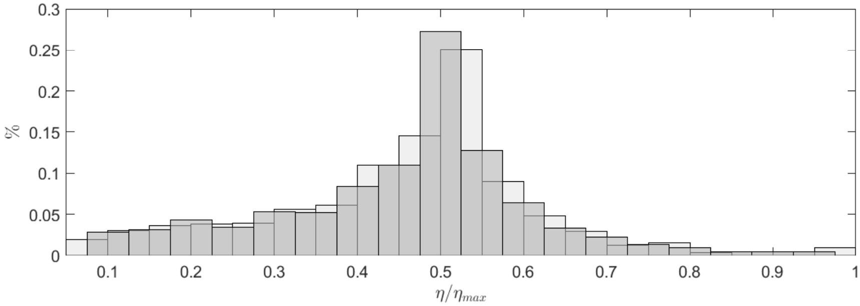

FIGURE S2. The histogram of dimensionless free surface elevations at CG1 (figure S1) for $L_p/h_0 = 20$ and $F_{in} = 1.3$.

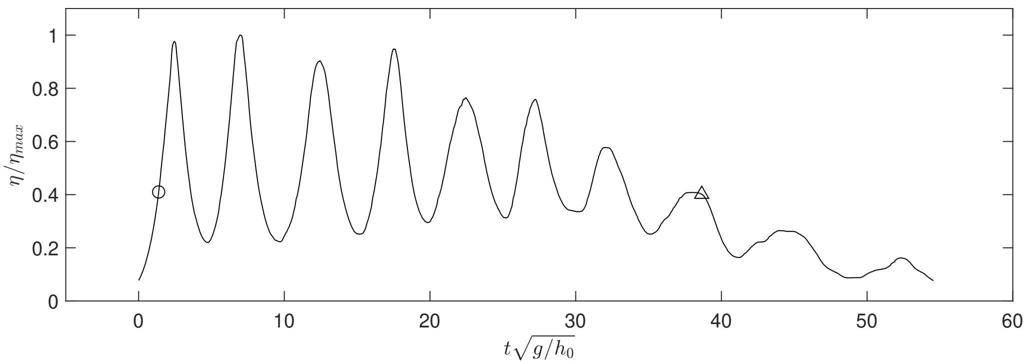

FIGURE S3. Time history of dimensionless free surface elevations at CG4 for $L_p/h_0 = 20$ and $F_{in} = 1.3$. Triangle marks the beginning of the bore tail and circle the first point with the same amplitude.

to reach CG2, resulting in a strength $F_{12} = 1.75$. The difference in bore strengths is produced by a difference in the arrival times of $0.56t\sqrt{g/h_0}$, which is considerably shorter than the bore front jump duration ($\approx 2t\sqrt{g/h_0}$). Given the fluctuations present on the breaking bore front the arrival times fluctuations are considered acceptable and, therefore, also the bore strength scattering.

The detail of the bore arrivals at CG5 and CG6 for cases $F_{in} = 1.1$ is shown in figure

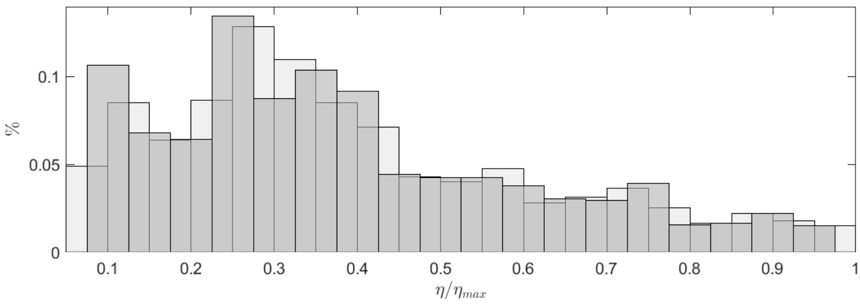

FIGURE S4. The histogram of dimensionless free surface elevations at CG4 (figure S3) for $L_p/h_0 = 20$ and $F_{in} = 1.3$.

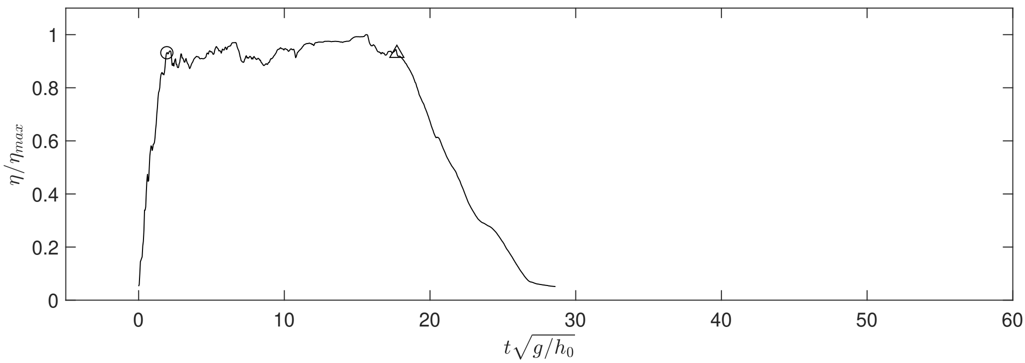

FIGURE S5. Time history of dimensionless free surface elevations at CG1 for $L_p/h_0 = 33.33$ and $F_{in} = 1.7$. Triangle marks the beginning of the bore tail and circle the first point with the same amplitude.

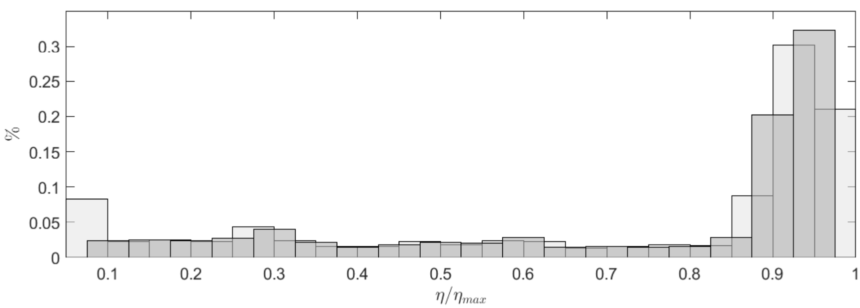

FIGURE S6. The histogram of dimensionless free surface elevations at CG1 (figure S5) for $L_p/h_0 = 33.33$ and $F_{in} = 1.7$.

S10. All the cases have been synchronized with the bore front arrival times at CG5. The case $L_p/h_0 = 26.67$ takes 6.06 $t\sqrt{g/h_0}$ to reach CG6 from CG5, resulting in a strength $F_{12} = 1.12$. The case $L_p/h_0 = 33.33$ takes 6.49 $t\sqrt{g/h_0}$ to reach CG6 from CG5, resulting in a strength $F_{12} = 1.02$. The difference in bore strengths is produced by a difference in the arrival times of $0.43t\sqrt{g/h_0}$, which seems negligible compared to the waves' front profile. Therefore, the bores strength scattering is also considered acceptable for these cases.

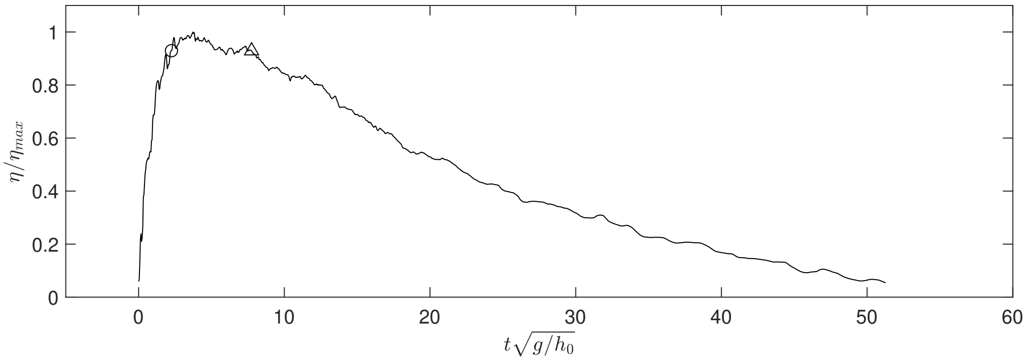

FIGURE S7. Time history of dimensionless free surface elevations at CG4 for $L_p/h_0 = 33.33$ and $F_{in} = 1.7$. Triangle marks the beginning of the bore tail and circle the first point with the same amplitude.

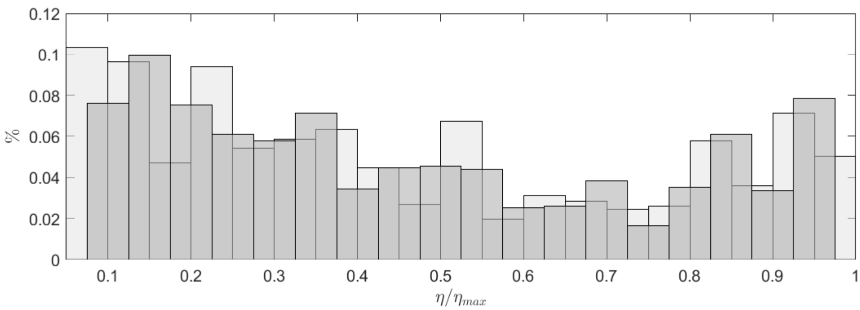

FIGURE S8. The histogram of dimensionless free surface elevations at CG4 (figure S7) for $L_p/h_0 = 33.33$ and $F_{in} = 1.7$.

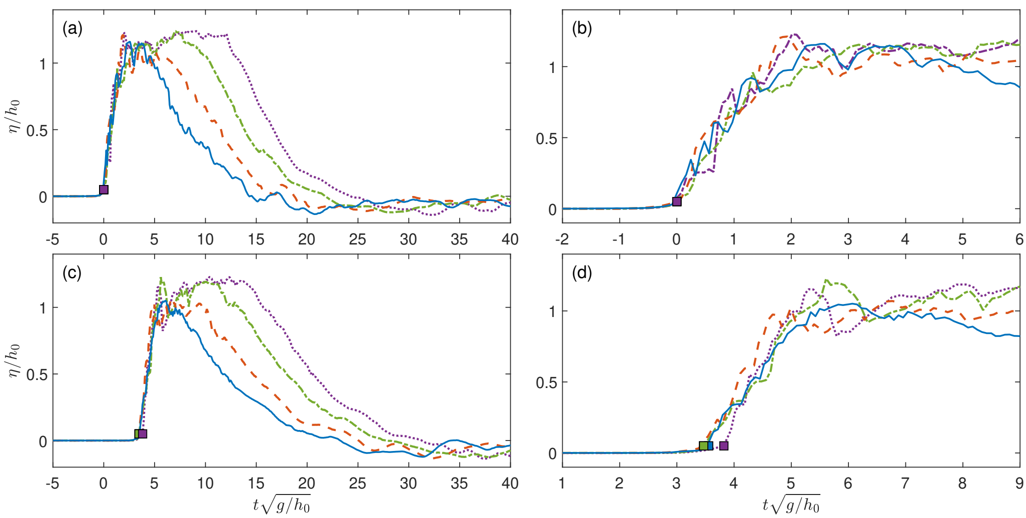

FIGURE S9. Time histories of dimensionless free surface elevations at CG1, on the top panels, and CG2, on the bottom panels, $F_{in} = 1.9$. Two views are presented. While the zoomed out view is shown on the left panels, the details of the bore front are shown on the right panels. Results for L_p/h_0=13.33 are plotted in blue; L_p/h_0=20 in orange; L_p/h_0=26.67 in green; and L_p/h_0=33.33 in purple lines. Squares represent the arrival of bore front.

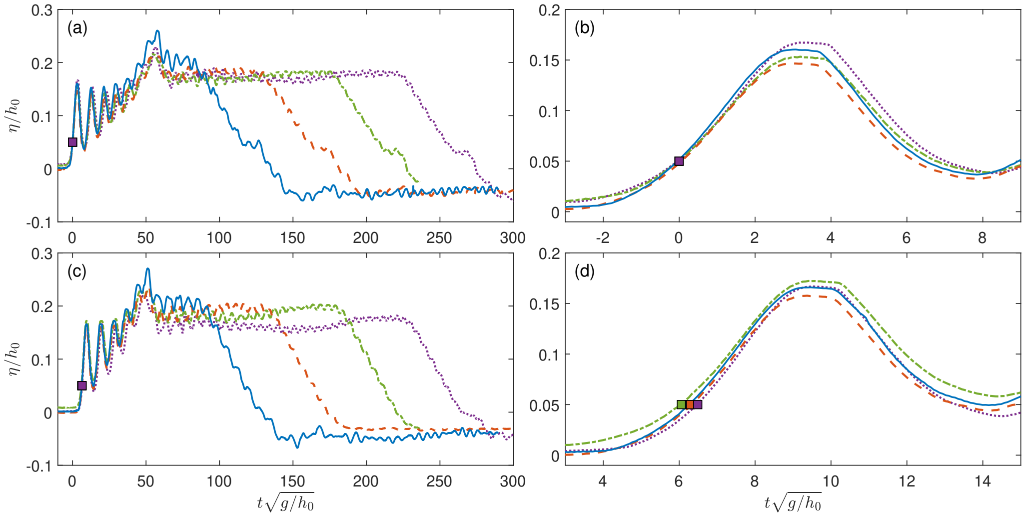

FIGURE S10. Time histories of dimensionless free surface elevations at CG5, on the top panels, and CG6, on the bottom panels, F_{in} = 1.2. Two views are presented. While the zoomed out view is shown on the left panels, the details of the bore front are shown on the right panels. Results for L_p/h_0=13.33 are plotted in blue; L_p/h_0=20 in orange; L_p/h_0=26.67 in green; and L_p/h_0=33.33 in purple lines. Squares represent the arrival of bore front.

S.3 HSPIV data convergence

The ensemble-averaged and fluctuating horizontal and vertical velocities measurements for F_{in} = 1.6 at fix locations and times are analyzed as functions of the number of repetitions in this section. The time history of the horizontal and vertical velocities for each repetition at $x = -9.87$ m are plotted in figures S11 and S12, respectively. The differences among the 10 repetitions are negligible initially for both horizontal and vertical velocities. Small variations among the repetitions are observed beginning at $t\sqrt{g/h_0} \approx -35$, triggered by the shear between horizontal and vertical velocities. At the breaking front, the fluctuating velocities first appear near the free surface and reach lower elevation in the water column after some duration. Oscillations in the horizontal and vertical velocities appear in the bottom boundary starting at $t\sqrt{g/h_0} \approx -32.5$.

Measurements of the vertical profiles of the ensemble-averaged flow velocities, calculated using 4, 7 and 10 repetitions, at $x = -9.92$ m and $t\sqrt{g/h_0} = -34.30$, 30.56 and -20.92, are plotted in figures S13, S14 and S15, respectively. In addition, the moving mean for the different measurements is calculated in windows of 5 data points. At the bore front toe ($t\sqrt{g/h_0} = -34.30$, figure S13), the ensemble-averaged flow velocities agree well, independent of the number of repetitions employed to calculate the ensemble-averaged values (with the exception of a couple of data points close to the free surface). Similarly, the horizontal flow velocities at the bore plateau ($t\sqrt{g/h_0} = -30.56$, figure S14) agree well with the exception of data points close to the free surface. The vertical velocities, which are one order of magnitude smaller than the horizontal velocities, show different trends below $z/h_0 = 0.9$ for 4 repetitions compared to the velocities for 7 and 10 repetitions. Close to the free surface the data shows large scatterings. The horizontal and vertical velocities at the bore tail ($t\sqrt{g/h_0} = -20.92$, figure S15) show similar repeatability to that observed at the bore plateau.

The relative differences between 3 and 4 repetitions, 6 and 7 repetitions and 9 and 10 repetitions for the ensemble-averaged flow velocity vertical profiles at $x = -9.92$ m and $t\sqrt{g/h_0} = -34.30$, 30.56 and -20.92, are plotted in figures S16, S17 and S18. The

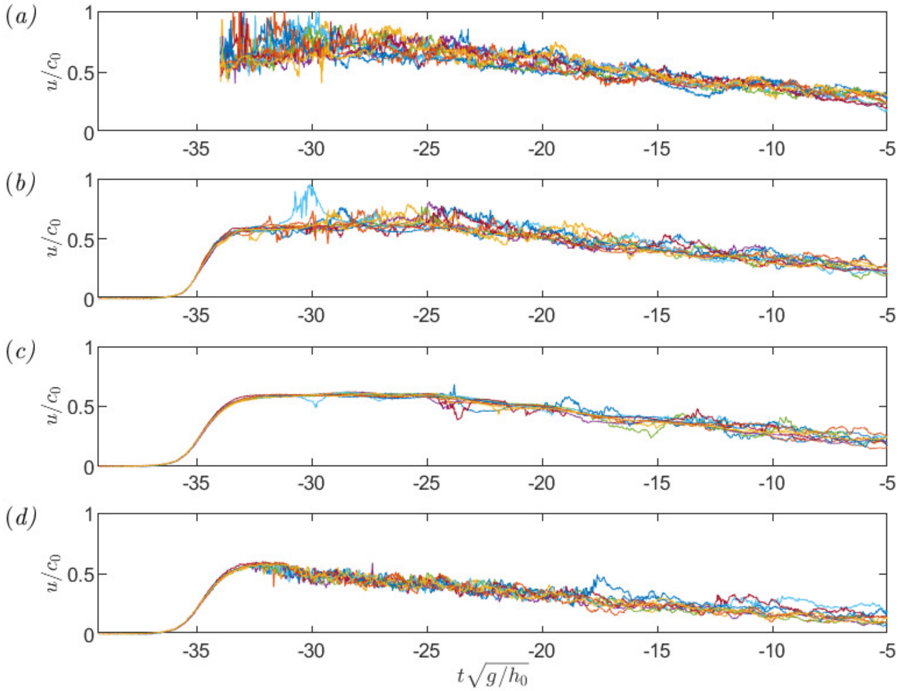

FIGURE S11. Time histories of horizontal velocities for each repetition at $x = -9.87$ m, $F_{in} = 1.6$. Panel (a) is for z/h_0=1.19; panel (b) is for z/h_0=0.80; panel (c) is for z/h_0=0.24; and panel (d) is for z/h_0=0.02;

ensemble-averaged horizontal velocities relative differences are calculated as

$$\overline{u}\% = \frac{(\overline{u_i} - \overline{u_j})}{\sqrt{\overline{u_i}^2 + \overline{w_i}^2}} 100, \tag{1.1}$$

where i and j are the number of repetitions, being i the largest. Equation (1.1) is used to calculate the relative differences for all the measurements from now by replacing the terms $\overline{u_i}$ and $\overline{u_j}$. The relative differences are smaller than 5% for more than 7 repetitions for both horizontal and vertical ensemble-averaged velocities. Relative differences increase near the free surface at the bore front toe ($t\sqrt{g/h_0} = -34.30$, figure S16). At the bore plateau ($t\sqrt{g/h_0} = -20.92$, figure S17) the relative differences are significantly larger above $z/h_0 = 1$. At the bore tail ($t\sqrt{g/h_0} = -20.92$, figure S17) relative differences are independent of the number of repetitions in the entire water column.

Measurements of the horizontal and vertical fluctuating velocity vertical profiles, calculated using 4, 7 and 10 repetitions, at $x = -9.92$ m and $t\sqrt{g/h_0} = -34.30$, 30.56 and -20.92, are plotted in figures S19, S20 and S21, respectively. The horizontal and vertical fluctuating velocities at the bore front toe ($t\sqrt{g/h_0} = -34.30$, figure S19) are independent of the number of repetitions except for the data points closer to the free surface. At the bore plateau (figure S20) although the moving means converge over more than 7 repetitions, the data still show scatterings for $z/h_0 > 0.8$. Similar behaviour is observed at the bore tail (figure S21).

The relative differences between 3 and 4 repetitions, 6 and 7 repetitions and 9 and

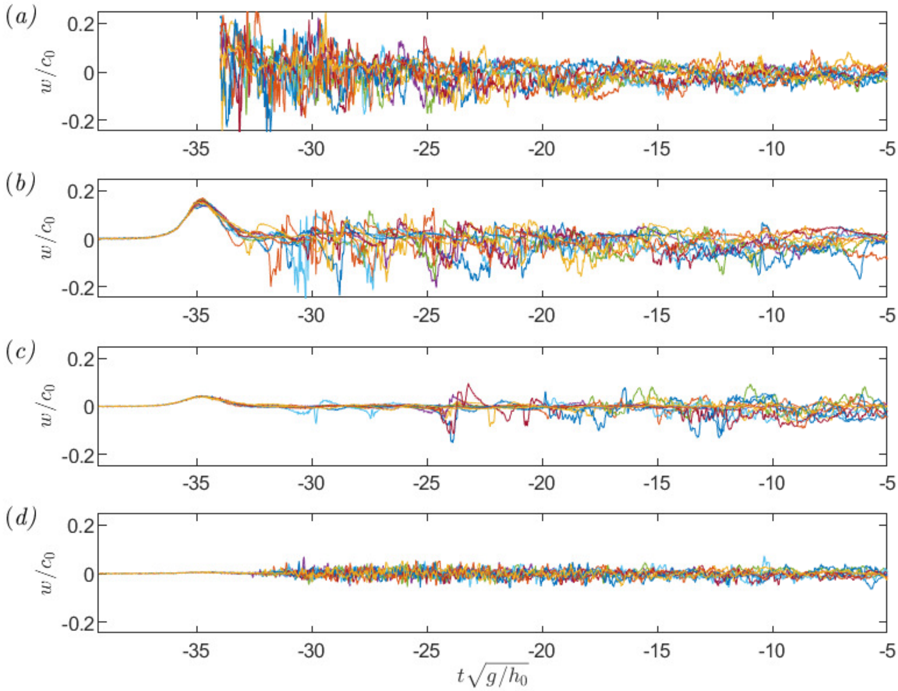

FIGURE S12. Time histories of vertical velocities for each repetition at $x = -9.87$ m, $F_{in} = 1.6$. Panel (a) is for z/h_0=1.19; panel (b) is for z/h_0=0.80; panel (c) is for z/h_0=0.24; and panel (d) is for z/h_0=0.02;

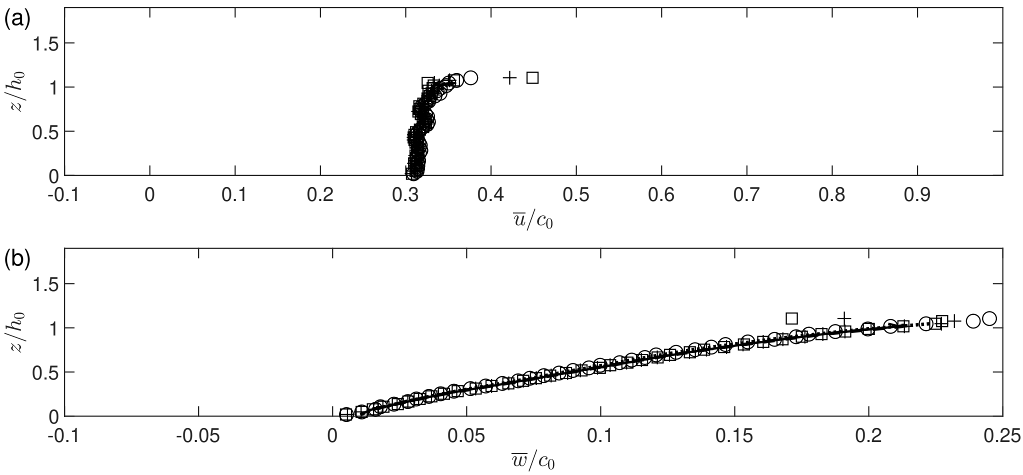

FIGURE S13. Vertical profiles of ensemble-averaged flow velocities in the water column at $x = -9.87$ m during the bore front toe ($t/\sqrt{g/h_0} = -34.30$). $F_{in} = 1.6$. (a) horizontal velocity component and (b) vertical velocity component. ○ and dotted line, 4 repetitions; + and dashed line, 7 repetitions; □ and solid line, 10 repetitions.

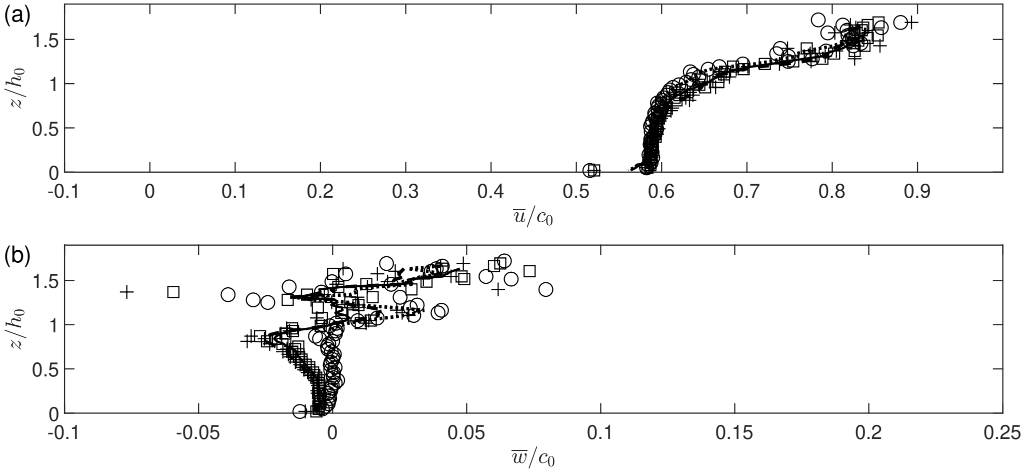

FIGURE S14. Vertical profiles of ensemble-averaged flow velocities in the water column at $x = -9.87$ m during the bore plateau ($t/\sqrt{g/h_0} = -30.56$). $F_{in} = 1.6$. (a) horizontal velocity component and (b) vertical velocity component. ○ and dotted line, 4 repetitions; + and dashed line, 7 repetitions; □ and solid line, 10 repetitions.

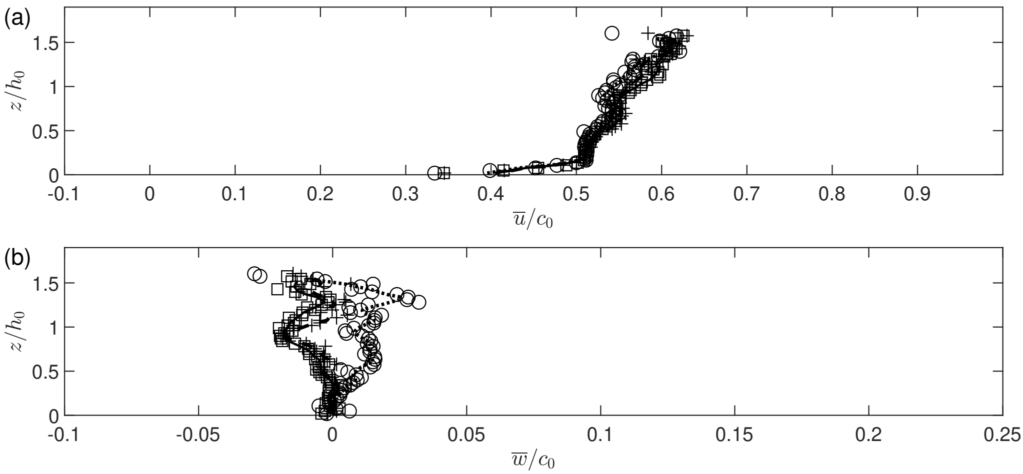

FIGURE S15. Vertical profiles of ensemble-averaged flow velocities in the water column at $x = -9.87$ m during the bore tail ($t/\sqrt{g/h_0} = -20.92$). $F_{in} = 1.6$. (a) horizontal velocity component and (b) vertical velocity component. ○ and dotted line, 4 repetitions; + and dashed line, 7 repetitions; □ and solid line, 10 repetitions.

10 repetitions for the fluctuating flow velocities vertical profiles at $x = -9.92$ m and $t\sqrt{g/h_0} = -34.30$, 30.56 and -20.92, are plotted in figures S22, S23 and S24. The relative differences are smaller than 4% for more than 7 repetitions for horizontal and vertical fluctuating velocities at the bore front and bore plateau. Similar to the ensemble-averaged flow velocities, considerable differences and scattering are observed at the bore plateau for $z/h_0 > 0.8$ and at the bore tail through the entire water column.

S.4 Spatial spectra of fluctuating velocities

Spatial spectrum analysis is carried out for the fluctuating velocities. Following Pope (2000), the one-sided energy spectrum is calculated as twice the square of the absolute

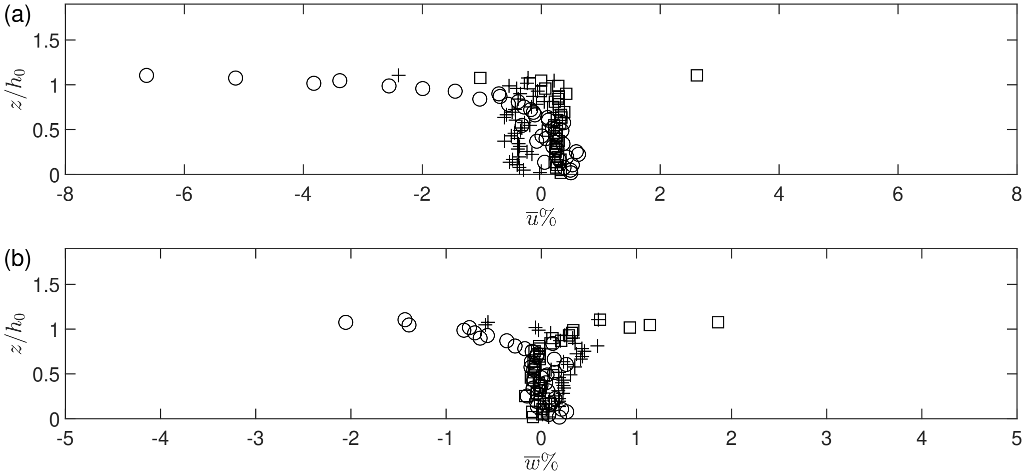

FIGURE S16. Vertical profiles of the ensemble-averaged flow velocities relative differences (in percentage) in the water column at $x = -9.87$ m during the bore front toe ($t/\sqrt{g/h_0} = -34.30$). $F_{in} = 1.6$. (a) horizontal velocity component and (b) vertical velocity component. ○ and dotted line, difference between 3 and 4 repetitions; + and dashed line, difference between 6 and 7 repetitions; □ and solid line, difference between 9 and 10 repetitions.

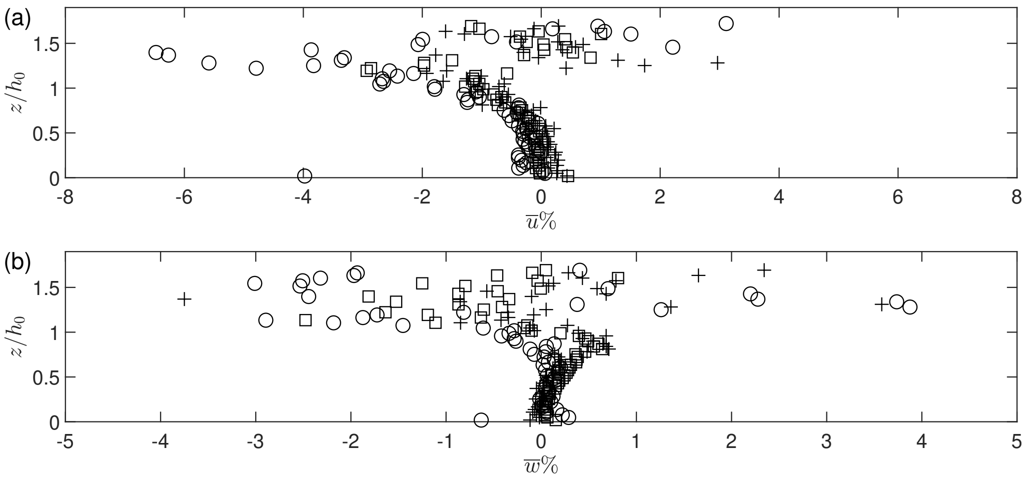

FIGURE S17. Vertical profiles of the ensemble-averaged flow velocities relative differences (in percentage) in the water column at $x = -9.87$ m during the bore plateau ($t/\sqrt{g/h_0} = -30.56$). $F_{in} = 1.6$. (a) horizontal velocity component and (b) vertical velocity component. ○ and dotted line, difference between 3 and 4 repetitions; + and dashed line, difference between 6 and 7 repetitions; □ and solid line, difference between 9 and 10 repetitions.

value of the Fourier transform of the fluctuating velocity along the horizontal direction at a given time and elevation (i.e., $E_{11}(t,\kappa_1,z) = 2|\mathcal{F}(u''(t,x,z))|^2$ and $E_{22}(t,\kappa_1,z) = 2|\mathcal{F}(w''(t,x,z))|^2$), where $u''(t,x,z) = u'(t,x,z) - \overline{u'}(t,z)$ and $w''(t,x,z) = w'(t,x,z) - \overline{w'}(t,z)$, and $\overline{u'}(t,z)$ and $\overline{w'}(t,z)$ are the mean fluctuating velocity components along x. The ensemble-averaged longitudinal and perpendicular spatial spectra, $\overline{E_{11}}$ and $\overline{E_{22}}$, are determined from 10 instantaneous one-dimensional spatial spectra.

Ensemble-averaged longitudinal and perpendicular spatial spectra for $F_{in} = 1.6$ at FOV1 are plotted in figure S25. The highest energy levels are observed near the bore front

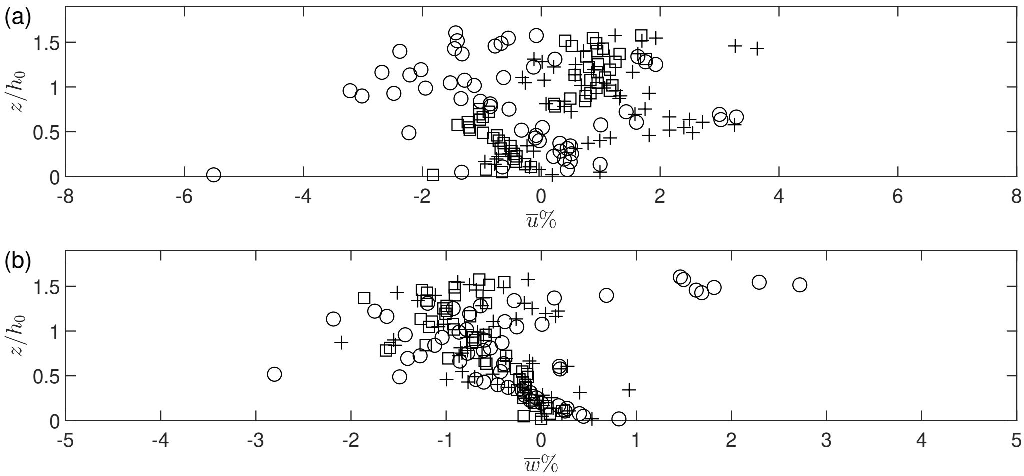

FIGURE S18. Vertical profiles of the ensemble-averaged flow velocities relative differences (in percentage) in the water column at $x = -9.87$ m during the bore tail ($t/\sqrt{g/h_0} = -20.92$). $F_{in} = 1.6$. (a) horizontal velocity component and (b) vertical velocity component. ○ and dotted line, difference between 3 and 4 repetitions; + and dashed line, difference between 6 and 7 repetitions; □ and solid line, difference between 9 and 10 repetitions.

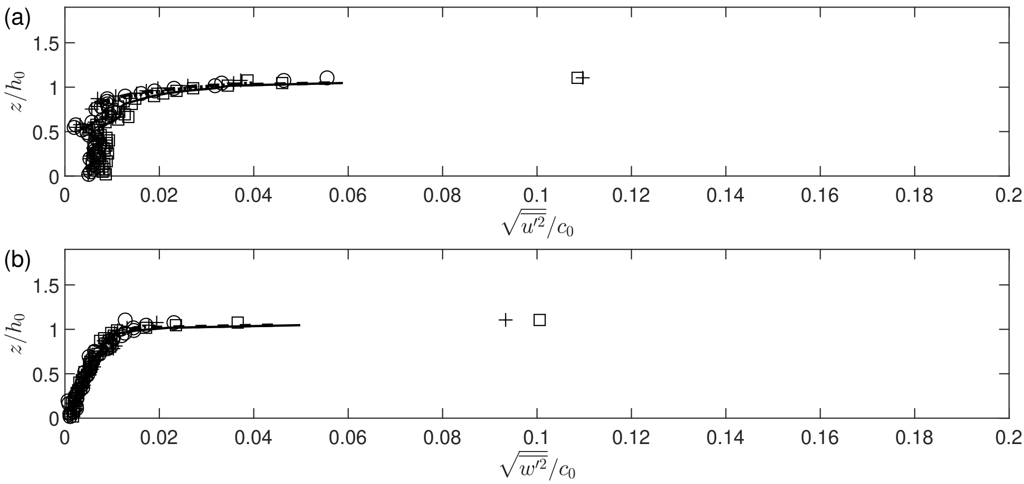

FIGURE S19. Vertical profiles of flow fluctuating velocities in the water column at $x = -9.87$ m during the bore front toe ($t/\sqrt{g/h_0} = -34.30$). $F_{in} = 1.6$. (a) the magnitude of horizontal fluctuating velocity component and (b) the magnitude of vertical fluctuating velocity component. ○ and dotted line, 4 repetitions; + and dashed line, 7 repetitions; □ and solid line, 10 repetitions.

(see panel (a)), in which the perpendicular and longitudinal spectra have power slope between -1 and -5/3. Noted that for homogeneous isotropic turbulence the spatial spectra follow a -5/3 power slope. On the other hand, the spatial spectra of turbulence in the wall boundary layer has a power slope of -1 in the inertial subrange for $(1/\mathscr{H}) \leqslant \kappa \leqslant (1/z)$, where the scale $\mathscr{H}$ is an external scale of the flow (Tchen 1954; Nikora 1999). In the present study, $\mathscr{H}$ is defined as the boundary layer thickness, estimated as the height of the first point from the bottom where the horizontal velocity is equal to or larger than 95% of the median of the velocities along the water column. Moreover, the -3 power slope characterizes a two-dimensional turbulence (Kraichnan 1967), which often exists

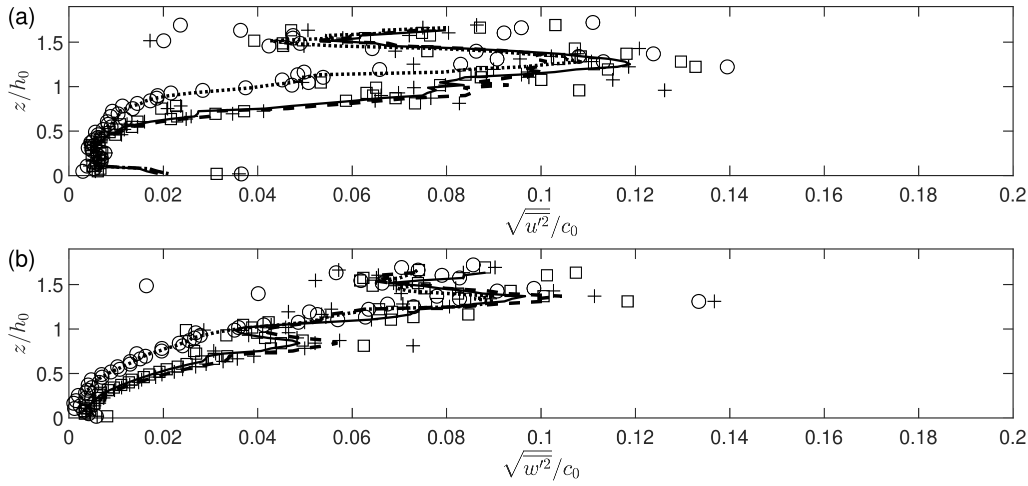

FIGURE S20. Vertical profiles of flow fluctuating velocities in the water column at $x = -9.87$ m during the bore plateau ($t/\sqrt{g/h_0} = -30.56$). $F_{in} = 1.6$. (a) the magnitude of horizontal fluctuating velocity component and (b) the magnitude of vertical fluctuating velocity component. ◯ and dotted line, 4 repetitions; + and dashed line, 7 repetitions; □ and solid line, 10 repetitions.

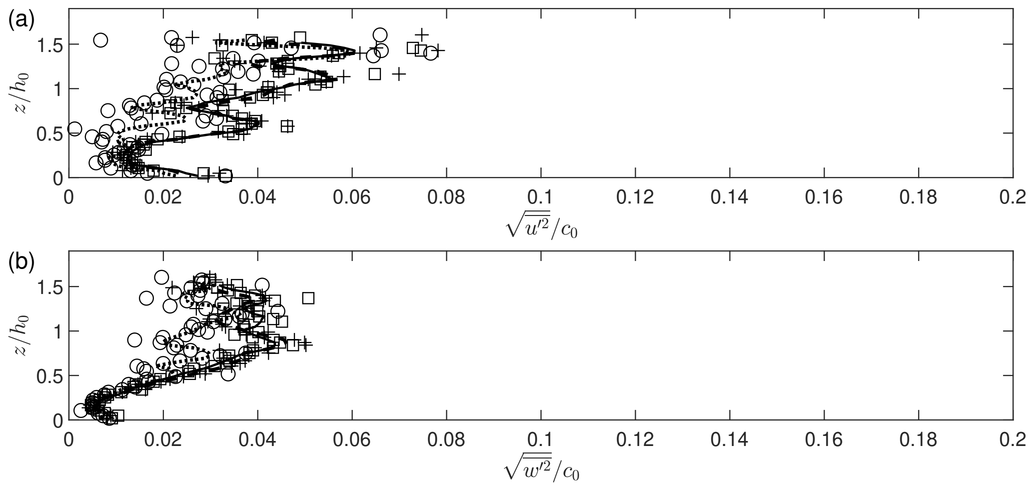

FIGURE S21. Vertical profiles of flow fluctuating velocities in the water column at $x = -9.87$ m during the bore tail ($t/\sqrt{g/h_0} = -20.92$). $F_{in} = 1.6$. (a) the magnitude of horizontal fluctuating velocity component and (b) the magnitude of vertical fluctuating velocity component. ◯ and dotted line, 4 repetitions; + and dashed line, 7 repetitions; □ and solid line, 10 repetitions.

in shallow flows with vertical confinement constraining large-scale turbulence structures to horizontal motions (Chen & Jirka 1995; Uijttewaal & Booij 2000; Uijttewaal & Jirka 2003). As shown in panel (g) in figure S25 the lowest energy levels are observed in between the breaking bore front and the bottom boundary. At this time and location, the fluctuating velocities are relatively small compared to those produced by the aerated breaking front. The spatial spectrum in panel (d) shows a slope close to -5/3 and with slightly lower energy level than that observed near the free surface of breaking front. The spectrum observed in panel (j) is captured near the bottom boundary. At this time and location the fluctuations observed near the breaking front have not reached yet the bottom boundary. The horizontal and vertical spectra follow a similar slope, close to -1

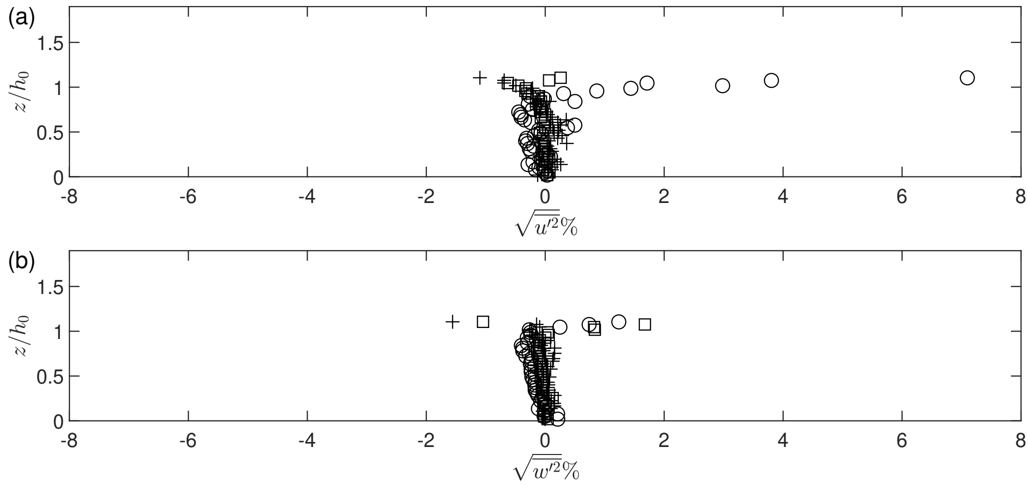

FIGURE S22. Vertical profiles of the flow fluctuating velocities relative differences (in percentage) in the water column at $x = -9.87$ m during the bore front ($t/\sqrt{g/h_0} = -34.30$). $F_{in} = 1.6$. (a) the magnitude of horizontal fluctuating velocity component and (b) the magnitude of vertical fluctuating velocity component. ◯, difference between 3 and 4 repetitions; +, difference between 6 and 7 repetitions repetitions; □, difference between 9 and 10 repetitions.

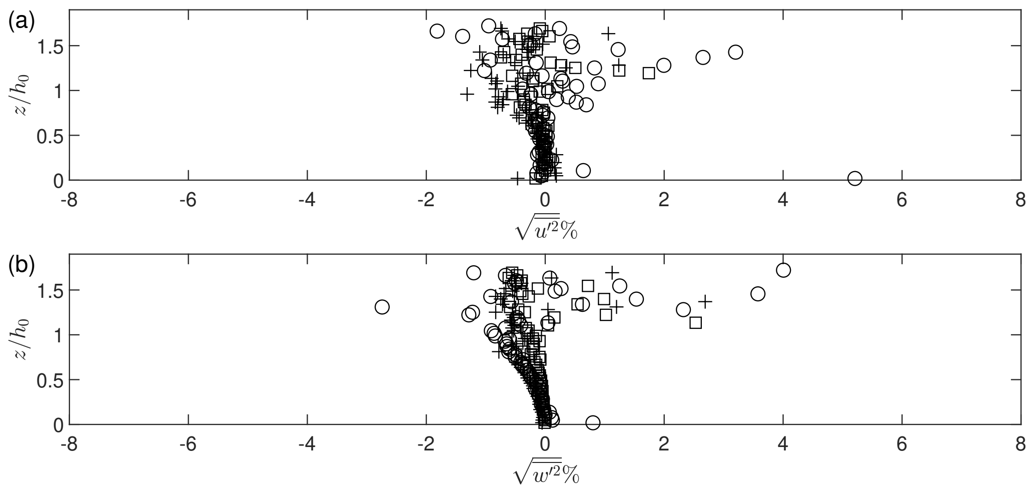

FIGURE S23. Vertical profiles of the flow fluctuating velocities relative differences (in percentage) in the water column at $x = -9.87$ m during the bore plateau ($t/\sqrt{g/h_0} = -30.56$). $F_{in} = 1.6$. (a) the magnitude of horizontal fluctuating velocity component and (b) the magnitude of vertical fluctuating velocity component. ◯, difference between 3 and 4 repetitions; +, difference between 6 and 7 repetitions repetitions; □, difference between 9 and 10 repetitions.

for $\kappa < 4\text{x}10^2$, which becomes steeper and close to -5/3 for the larger wavenumbers. On the other hand, the spectrum in the horizontal direction is more energetic. The spatial spectra are similar along the water column above the bed boundary layer during the bore tail (panels (b), (e), (h), (f) and (i)), with a slope close to -5/3 along the entire wavenumber domain. It can also be observed that the spectrum energy decreases in time (panels (d), (e) and (f)). At panels (k) and (l), near the bottom boundary, the spectra show a similar trend: its slope is milder slope at low wavenumbers and steepens smoothly at larger wavenumbers.

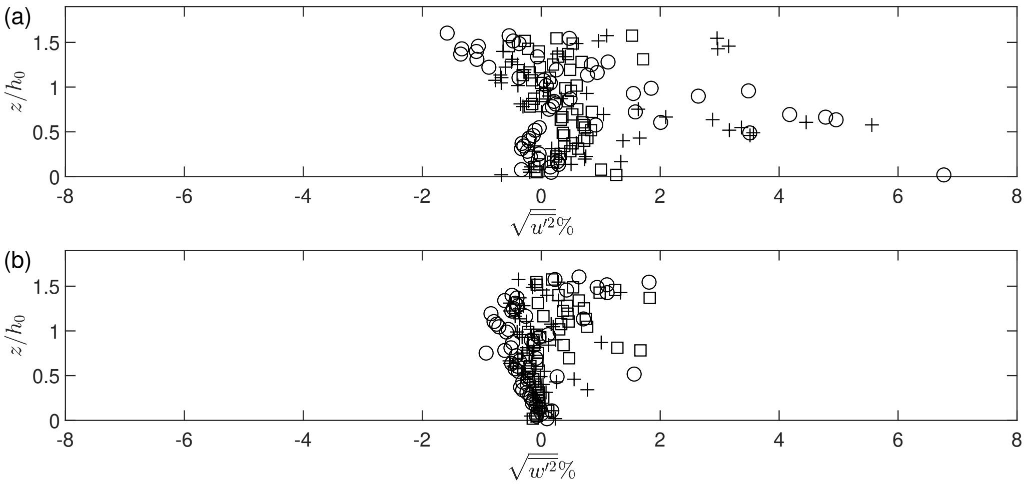

FIGURE S24. Vertical profiles of the flow fluctuating velocities relative differences (in percentage) in the water column at $x = -9.87$ m during the bore tail ($t/\sqrt{g/h_0} = -20.92$). $F_{in} = 1.6$. (a) the magnitude of horizontal fluctuating velocity component and (b) the magnitude of vertical fluctuating velocity component. ○, difference between 3 and 4 repetitions; +, difference between 6 and 7 repetitions repetitions; □, difference between 9 and 10 repetitions.

The ensemble-averaged longitudinal and perpendicular spatial spectra for $F_{in} = 1.1$ at FOV2 are plotted in figure S26. During the backwash of the third undulation, fluctuating velocities have a similar magnitude in the entire water column (panels (a), (d), (g) and (j)). A change in the power slope is observed around $\kappa \approx 10^2$, from a slope milder than -1 to a slope in between -5/3 and -3. On the 5th undulation (panels (b), (e), (h) and (k)) the energy spectra level has decreased and the power slope at larger wavenumbers has become slightly milder. The spatial spectra reach the lowest energy levels at $t\sqrt{g/h_0} \approx 90$ (panels (c), (f), (i) and (l)), and remains practically unchanging for the rest of the swash event, including the bore rundown. During this phase the spectra values for E_{11} and $4/3E_{22}$ are similar and have an almost constant slope throughout the entire spectra, with a power slope $\approx -5/3$. The spectra are constant through the water column with the exception of the spectra right above the slope (panel (l)). Near the bottom boundary, differences between the longitudinal and perpendicular spectra are generally observed for the largest scales (smallest wavenumbers). However, differences are also observed for the smallest scales before the third undulation (panel (j)). While the perpendicular spectrum has a mild power slope, which becomes steeper for $\kappa > 10^2$, the longitudinal spectrum follows an opposite trend; i.e., the slope of the longitudinal spectrum is milder for $\kappa > 10^2$. This behaviour is also observed, to a lesser extent, in panel (k).

The ensemble-averaged longitudinal and perpendicular spatial spectra for $F_{in} = 1.6$ at FOV2 are plotted in figure S27. The bore reaches FOV2 with energy levels similar to the observed near the bore front in the constant water depth. Near the bottom boundary layer (panel (j)), noticeable differences between the longitudinal and perpendicular spectra are observed for the lowest and largest wavenumber, similar to the observed during the UB 3rd undulation rundown at FOV2. At the flow reversal stage (panels (b), (e), (h) and (k)) the spectra are similar to the spectra observed at FOV 1 after the bore has passed: spectra with power slope approximately -5/3 at the largest wavenumbers with differences between the spectra near the bottom boundary for the smallest wavenumbers. During the bore rundown (panels (f), (i) and (l)) differences between the longitudinal and perpendicular spectra are observed for the entire wavenumber range at the three depth levels.

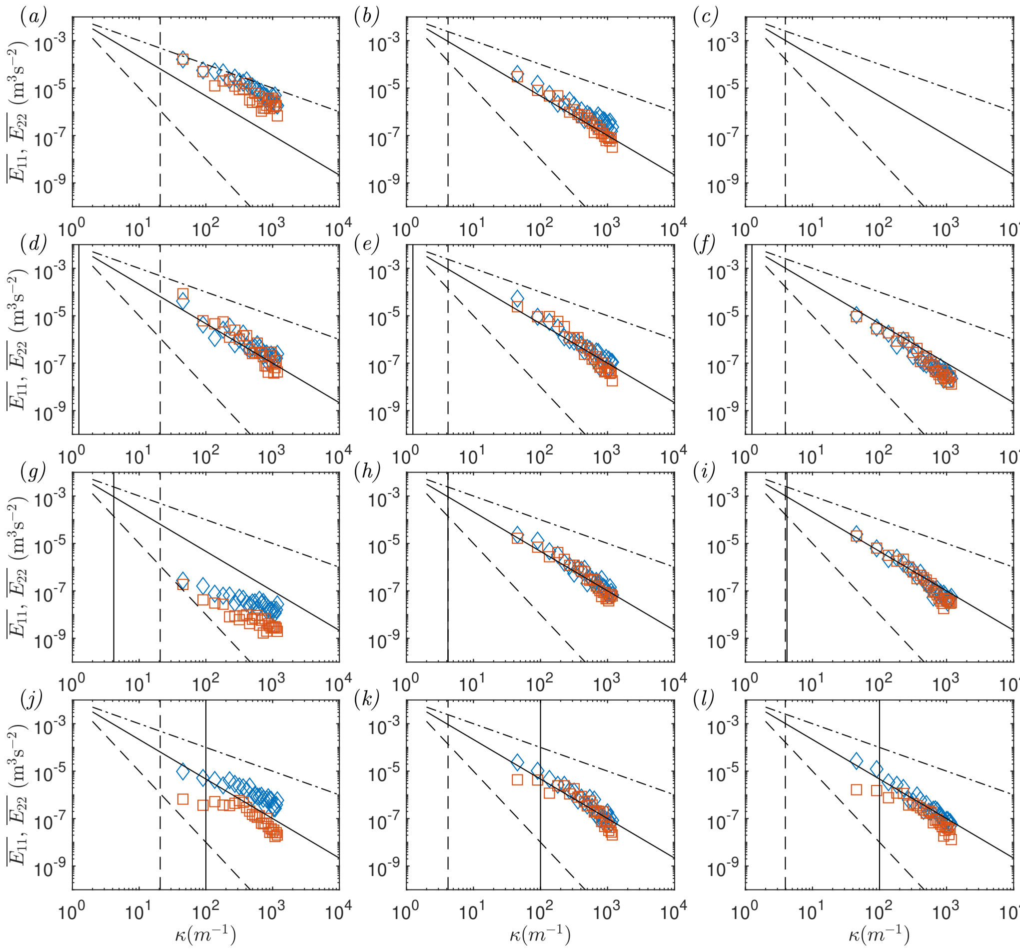

FIGURE S25. Spatial spectra measurements at different time and elevation for the BB with $F_{in} = 1.6$ at FOV1. The first column (panels (a), (d), (g) and (j)) is for $t\sqrt{g/h_0} = -31$; the second column (panels (b), (e), (h) and (k)) for $t\sqrt{g/h_0} = -10$; and the third column (panels (c), (f), (i) and (l)) for $t\sqrt{g/h_0} = 10$. The first row denotes $z/h_0 = 1.19$; the second row $z/h_0 = 0.80$; the third row $z/h_0 = 0.24$ and the fourth row $z/h_0 = 0.02$. $\diamond$ and $\square$ represent $\overline{E_{11}}$ and $4/3\overline{E_{22}}$, respectively. Dashed-dotted power slope is -1, solid line power slope is -5/3 and dashed line power slope is -3. Vertical solid line is located at $\kappa = 1/z$ and vertical dashed line at $\kappa = 1/\mathscr{H}$.

As mentioned before, the lack of information on the velocity component in the spanwise direction hinders the analysis of the turbulence fields. Also, spatial spectra observations are limited by the resolution and range of measurements. Most of the spectra only show the characteristics typical of the inertial sub-range, making it difficult to consistently define the limits between the energy containing range, the inertial sub-range and the dissipation range. Because of these reasons, the spatial spectrum analysis presented herein cannot truly characterize the turbulence properties.

REFERENCES

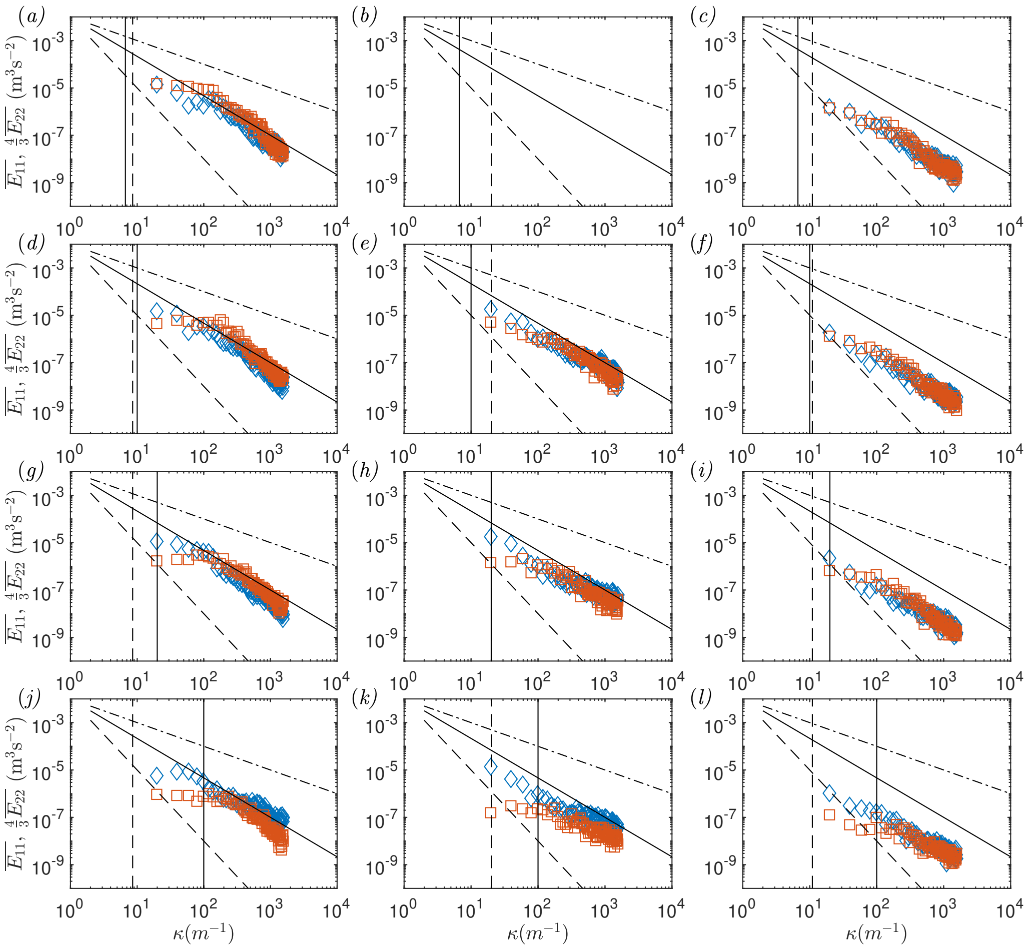

FIGURE S26. Spatial spectra measurements at different time and elevation for the UB with $F_{in} = 1.1$ at FOV2. The first column (panels (a), (d), (g) and (j)) is for $t\sqrt{g/h_0} = 33$; the second column (panels (b), (e), (h) and (k)) for $t\sqrt{g/h_0} = 50$; and the third column (panels (c), (f), (i) and (l)) for $t\sqrt{g/h_0} = 90$. The first row denotes $Z/h_0 = 0.14$; the second row $Z/h_0 = 0.1$; the third row $Z/h_0 = 0.05$ and the fourth row $Z/h_0 = 0.01$. $\diamond$ and $\square$ represent $\overline{E_{11}}$ and $4/3\overline{E_{22}}$, respectively. Dashed-dotted power slope is -1 slope, solid line power slope is -5/3 and dashed line power slope is -3. Vertical solid line is located at $\kappa = 1/Z$ and vertical dashed line at $\kappa = 1/\mathscr{H}$.

BARRANCO, I. & LIU, P. L.-F. 2021 Run-up and inundation generated by non-decaying dam-break bores on a planar beach. *Journal of Fluid Mechanics* **915**, A81.

CHEN, D. & JIRKA, G. H. 1995 Experimental study of plane turbulent wakes in a shallow water layer. *Fluid Dynamics Research* **16** (1), 11–41.

KRAICHNAN, R. H. 1967 Inertial ranges in two-dimensional turbulence. *The Physics of Fluids* **10** (7), 1417–1423.

NIKORA, V. 1999 Origin of the "−1" spectral law in wall-bounded turbulence. *Phys. Rev. Lett.* **83**, 734–736.

POPE, STEPHEN B. 2000 *Turbulent Flows*. Cambridge University Press.

TCHEN, C.-M. 1954 Transport processes as foundations of the heisenberg and obukhoff theories of turbulence. *Phys. Rev.* **93**, 4–14.

UIJTTEWAAL, W. S. J. & BOOIJ, R. 2000 Effects of shallowness on the development of free-surface mixing layers. *Physics of Fluids* **12** (2), 392–402.

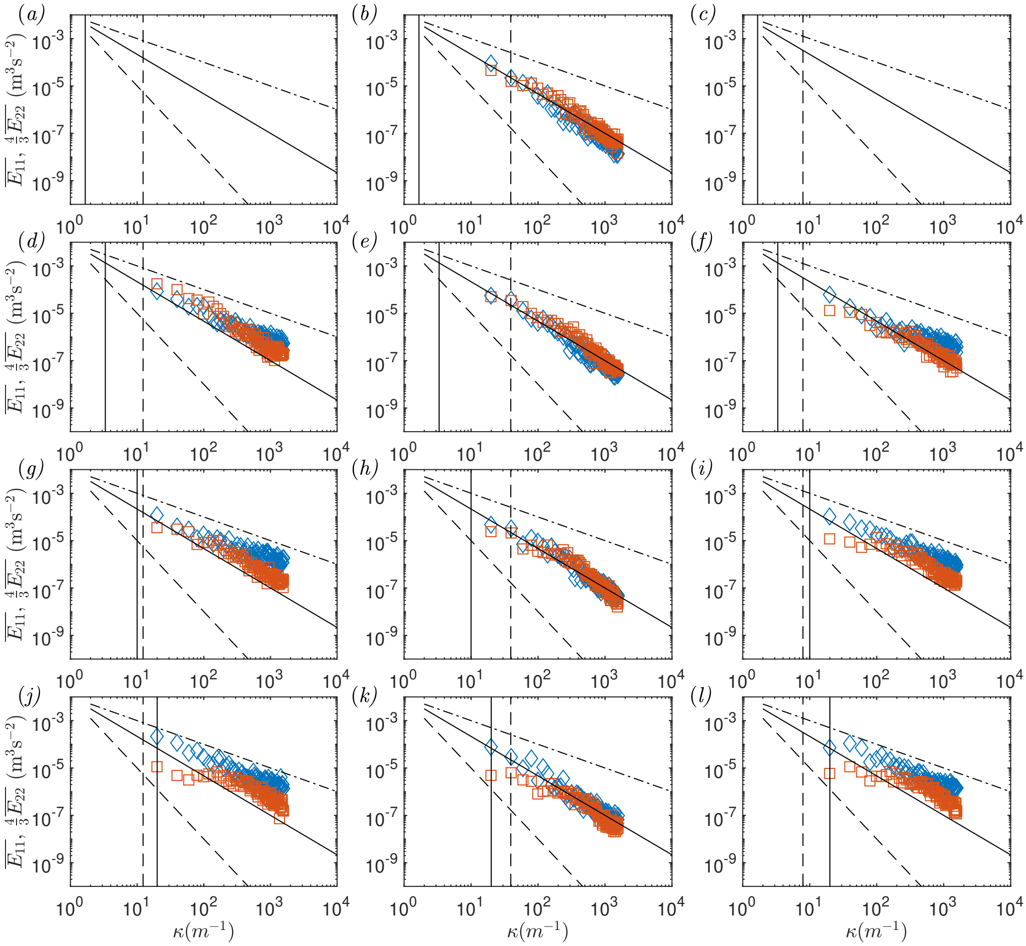

FIGURE S27. Spatial spectra measurements at different time and elevation for the BB with $F_{in} = 1.6$ at FOV2. The first column (panels (a), (d), (g) and (j)) is for $t\sqrt{g/h_0} = 15$; the second column (panels (b), (e), (h) and (k)) for $t\sqrt{g/h_0} = 30$; and the third column (panels (c), (f), (i) and (l)) for $t\sqrt{g/h_0} = 45$. The first row denotes $Z/h_0 = 0.60$; the second row $Z/h_0 = 0.29$; the third row $Z/h_0 = 0.09$ and the fourth row $Z/h_0 = 0.04$. $\diamond$ and $\square$ represent $\overline{E_{11}}$ and $4/3\overline{E_{22}}$, respectively. Dashed-dotted power slope is -1 slope, solid line power slope is -5/3 and dashed line power slope is -3. Vertical solid line is located at $\kappa = 1/z$ and vertical dashed line at $\kappa = 1/\mathscr{H}$.

UIJTTEWAAL, W. S. J. & JIRKA, G. H. 2003 Grid turbulence in shallow flows. *Journal of Fluid Mechanics* **489**, 325–344.